The Astrophysical Journal Letters, 756:L36 (5pp), 2012 September 10 doi:10.1088/2041-8205/756/2/L36


# SLOW MAGNETOACOUSTIC OSCILLATIONS IN THE MICROWAVE EMISSION OF SOLAR FLARES

S. Kim[1], V. M. Nakariakov[2,3], and K. Shibasaki[1]
[1] Nobeyama Solar Radio Observatory/NAOJ, Nagano 384-1305, Japan; sjkim@nro.nao.ac.jp
[2] Physics Department, University of Warwick, Coventry, CV4 7AL, UK
[3] Central Astronomical Observatory of the Russian Academy of Sciences at Pulkovo, 196140 St Petersburg, Russia
*Received 2012 May 25; accepted 2012 July 31; published 2012 August 23*

## ABSTRACT

Analysis of the microwave data, obtained in the 17 GHz channel of the Nobeyama Radioheliograph during the M1.6 flare on 2010 November 4, revealed the presence of 12.6 minute oscillations of the emitting plasma density. The oscillations decayed with the characteristic time of about 15 minutes. Similar oscillations with the period of about 13.8 minutes and the decay time of 25 minutes are also detected in the variation of EUV emission intensity measured in the 335 Å channel of the *Solar Dynamics Observatory*/Atmospheric Imaging Assembly. The observed properties of the oscillations are consistent with the oscillations of hot loops observed by the *Solar and Heliospheric Observatory*/Solar Ultraviolet Measurement of Emitted Radiation (SUMER) in the EUV spectra in the form of periodic Doppler shift. Our analysis presents the first direct observations of the slow magnetoacoustic oscillations in the microwave emission of a solar flare, complementing accepted interpretations of SUMER hot loop oscillations as standing slow magnetoacoustic waves.

*Key words:* Sun: corona – Sun: flares – Sun: oscillations – Sun: radio radiation

*Online-only material:* color figure

## 1. INTRODUCTION

Quasi-periodic pulsations (QPP) in the emission generated in solar flares, with the periods ranging from a fraction of a second to several minutes, have been intensively studied for several decades (see, e.g., Nakariakov & Melnikov 2009 for a recent review). One of the possibilities opened up by revealing the nature of QPP in flares is the diagnostics of physical conditions in flaring sites and mechanisms operating in them. Moreover, these diagnostics can be extended to stellar flares, which are also observed to have QPP in their radio, optical, and soft X-ray light curves (e.g., Stepanov et al. 2001; Mathioudakis et al. 2003; Mitra-Kraev et al. 2005; Pandey & Srivastava 2009). The origin of QPP is still not clear, while it is accepted that they can be produced by several mechanisms. Perhaps, one of the most understood possibility is the generation of QPP by magnetohydrodynamic (MHD) oscillations of coronal structures. Coronal MHD oscillations are clearly seen in various bands directly with modern high time and spatial resolution instruments, which provide researchers with the basis for identification in the flaring emission.

Standing longitudinal oscillations of coronal loops were first detected as the periodic Doppler shift of the emission lines Fe XIX and Fe XXI, with the formation temperature greater than 6 MK, with the *Solar and Heliospheric Observatory*/Solar Ultraviolet Measurement of Emitted Radiation (SUMER) instrument (Wang et al. 2003a, 2003b). The mean observed oscillation period is $17.6 \pm 5.4$ minutes. The oscillations are strongly damped, with the damping time about one period of the oscillation. In some cases, the intensity oscillations are seen. There is a quarter-period phase lag between the intensity and the Doppler shift oscillations. The oscillations are usually observed in association with the soft X-ray brightenings, sometimes up to the M-class flares (Wang et al. 2007). Similar Doppler-shift oscillations during solar flares in emission lines of S XV and Ca XIX, with the formation temperature 12–14 MK, observed with *Yohkoh*/BCS were reported by Mariska (2006, 2005). In cooler coronal emission lines, similar oscillations were detected with *Hinode*/EIS (Mariska et al. 2008; Srivastava & Dwivedi 2010).

The compressible nature of the longitudinal oscillations and their long periods led to their interpretation in terms of standing slow magnetoacoustic oscillations damped due to high thermal conduction (Ofman & Wang 2002). A series of numerical studies (e.g., Nakariakov et al. 2004; Mendoza-Briceño et al. 2004; Tsiklauri et al. 2004; Selwa et al. 2005; Taroyan et al. 2005; Ogrodowczyk & Murawski 2007; Selwa et al. 2007; Gruszecki & Nakariakov 2011), accounting for various additional physical effects including viscosity, two-dimensional and three-dimensional geometry, stratification, nonlinear steepening, and mode coupling, demonstrated the robustness of this interpretation. In particular, the simulations showed that, depending upon whether the oscillations are triggered at one or both footpoints of a coronal loop, the fundamental mode and its second spatial harmonics can be effectively excited (Nakariakov et al. 2004; Tsiklauri et al. 2004). The modes have different structures of the oscillations at the loop apex: in the fundamental mode there is a node of the density perturbation and the maximum of the field-aligned velocity perturbation at the apex, while it is the other way around in the second harmonics (see, e.g., Nakariakov & Melnikov 2006). The phase speed of the longitudinal (slow magnetoacoustic) waves is the tube speed $C_T = C_s C_A/\sqrt{C_s^2 + C_A^2}$, where $C_s$ and $C_A$ are the sound and Alfvén speeds, respectively (see, e.g., Roberts 2006; Wang 2011). The tube speed is subsonic and sub-Alfvénic. In a low-beta plasma the tube speed is just slightly lower than the sound speed, while in the case $C_s = C_A$ the tube speed decreases to about $0.7C_s$. With the decrease in the Alfvén speed $C_A < C_s$ the tube speed remains lower than the Alfvén speed.

Slow magnetoacoustic oscillations can be also observed in the non-thermal emission of solar and stellar flares. The possible mechanisms are the periodic triggering of magnetic reconnection by the modulation of the physical conditions in the vicinity of the reconnection site (Chen & Priest 2006), the modification of the spectral maximum of the gyrosynchrotron

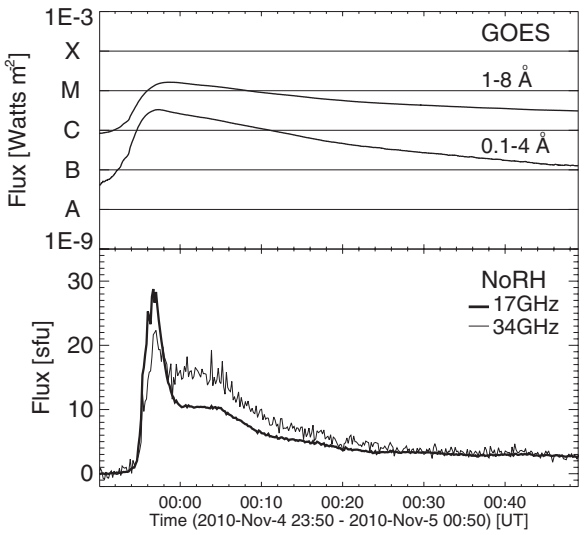


**Figure 1.** Time profile of *GOES* X-ray (top) and NoRH 17 and 34 GHz (bottom) flux during an M1.6 flare occurred on 2010 November 4. NoRH flux at each frequency is estimated over the field of view of Figure 2.

emission in the regime of the Razin suppression because of the periodic modulation of the electron plasma frequency (Nakariakov & Melnikov 2006), and the direct modulation of the emission intensity because of the change of the concentration of the emitting plasma. However, so far these theoretical possibilities have been without observational confirmation. In this Letter, we demonstrate, for the first time, the presence of longitudinal oscillations in the free–free microwave emission in a solar flare.

## 2. OBSERVATIONS

We have examined the flare loops produced by an M1.6 flare which occurs at the southeast limb on 2010 November 4. For this study, we used 17 GHz and 34 GHz data observed with Nobeyama Radioheliograph (NoRH; Nakajima et al. 1994; Takano et al. 1997) and 335 Å EUV data observed with the Atmospheric Imaging Assembly (AIA; Lemen et al. 2012) on board the *Solar Dynamics Observatory* (*SDO*). Microwave data have a spatial resolution of 10″ and a time cadence of 10 s. AIA data have a spatial resolution of 1.″2 and a 12 s time cadence. AIA 335 Å channel contains a contribution from Fe XVI with the peak-forming temperature of 2.5 MK for the flare (Lemen et al. 2012).

Figure 1 shows time profiles of the flare in soft X-rays taken with *GOES* satellite (top) and radio fluxes at 17 and 34 GHz (bottom). The flare starts at 23:55, peaks at 23:57 UT, and then gradually decays. The fluxes at 17 and 34 GHz vary with the same pattern during flare process but the difference of scale between them clearly changes as follows: for the flare peak, the 17 GHz flux is larger than the 34 GHz one and then decreases to less than 34 GHz, and finally both fluxes become comparable with each other. It implies that only in the flare peak is the radio emission generated by gyrosynchrotron motion of accelerated electrons, while in the long decay phase, thermal free–free dominate the radio emission. The Nobeyama Radiopolarimeter (NoRP; Nakajima et al. 1985), which observes the Sun in the 1, 2, 3.75, 9.4, 17, and 35 GHz channels, supports it with the same aspect at the high frequencies where the plasma becomes optically thin.

In Figure 2, we present spatial features of radio emission sources associated with the flare loops. Figure 2(a) shows the AIA 335 Å image taken at 00:30 UT and the brightness temperature ($T_B$) contours of NoRH 17 and 34 GHz. Figure 2(b) shows NoRH 17 GHz $T_B$ map with a contour of EUV flare loops observed by AIA 335 Å channel. The flare loops coincide with the microwave source. The top of the flare loops emanate strong EUV emission continuously throughout the whole flare. In Figure 3, we plot the variation of the maximum counts recorded in the AIA 335 Å channel for the flare region. Since the top of the flare loops is the dominant source during the flare, this plot reflects the intensity variation of the flare loop top. Interestingly, it shows an obvious decaying oscillation pattern after the flare peak time. Periodogram analysis of the signal (see, e.g., Scargle 1982), performed after removal of the linear trend, shows a clear spectral peak near 1.2 mHz and a secondary, less pronounced, peak near 2.4 mHz. The decay time is about 1500 s. Unfortunately, we could not confirm it in AIA 131 and 94 Å channel, where the peak of the temperature response is higher than 7 MK, due to the saturation effect on the top of the flare loops.

The NoRH observation at two frequencies allows us to derive a spectral index $\alpha$ for a spatially resolved region such as the loop top or loop footpoint. The index $\alpha$ is given by the ratio of the fluxes obtained at 17 and 34 GHz, $\alpha = \log(F_{17\,\mathrm{GHz}}/F_{34\,\mathrm{GHz}})/\log(17/34)$. For the top of the arcade (the white box in Figure 2(b)), the derived index $\alpha$ is close to 0 within the range of $-0.2 \sim 0.7$ during the decay phase. It implies that the radio emission in this region comes from an optically thin plasma (Dulk 1985).

We estimated the plasma temperature of the flare loops using the ratio of the two *GOES* channels (1–8 Å and 0.5–4 Å). Although the *GOES* satellite observes the full Sun, it is reasonable to use it in our analysis because this flaring loop is the only predominant source for increasing the X-ray flux during the flare time. Using *GOES* widget, we derived the temperature in the flare loops (White et al. 2005). The temperature response function of each filter is derived using the coronal abundances in CHIANTI 6.0.1 (Dere et al. 1997, 2009). The estimated peak temperature is 18 MK. Then, the temperature gradually decreases to about 7 MK (the top panel of Figure 4). Since we are focusing on the top of the flare loops that appears in microwave imaging data, we do not use the *GOES* emission measure estimated over the whole flare.

## 3. ELECTRON DENSITY

To derive the electron number density of the flare loop-top region, we used the brightness temperature obtained at 17 GHz of NoRH and the estimated plasma temperature by the two *GOES* channels. Based on the observations, we assume that in the top of the flare loops the free–free emission from the optically thin thermal plasma (the optical depth $\tau_\nu \ll 1$) is dominant. According to the radiative transfer at the radio frequency (e.g., Dulk 1985), the relation between the brightness temperature $T_B$ and the plasma temperature $T$ is given as

$$T_B = T\tau_\nu, \tag{1}$$

where $\tau_\nu$ is

$$\tau_\nu = \frac{9.786 \times 10^{-3}}{\nu^2} \log \Lambda \frac{\mathrm{EM}}{T^{3/2}}. \tag{2}$$

EM is the emission measure ($\mathrm{EM} = \int_z N^2 dz$) and $\log\Lambda$ is the Coulomb logarithm ($\log\Lambda = \log[4.7 \times 10^{10}(T/\nu)]$).

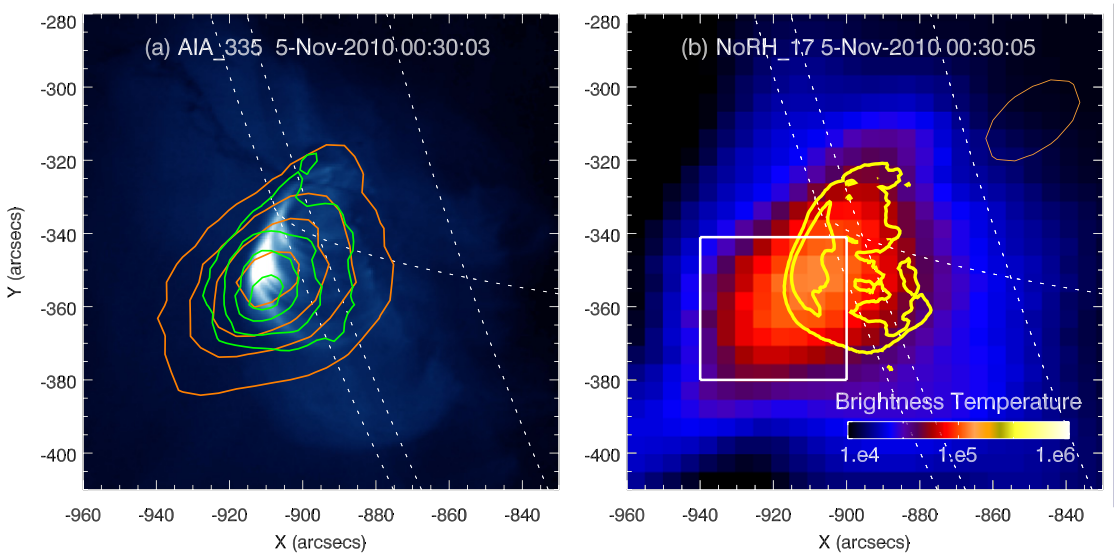


**Figure 2.** Images for the flare loops at around 00:30 UT on 2010 November 5. (a) AIA 335 Å channel image with contours of $T_B$ at NoRH 17 GHz (orange) and 34 GHz (green). The levels of the contours are 35, 55, 75, and 95% of the peak $T_B$ for each frequency. (b) NoRH 17 GHz $T_B$ map with the contour of the flare loop arcade observed by the AIA 335 Å channel. A beam size at 17 GHz appears in a yellow circle and a white box indicates the region where the electron density is estimated.

(A color version of this figure is available in the online journal.)

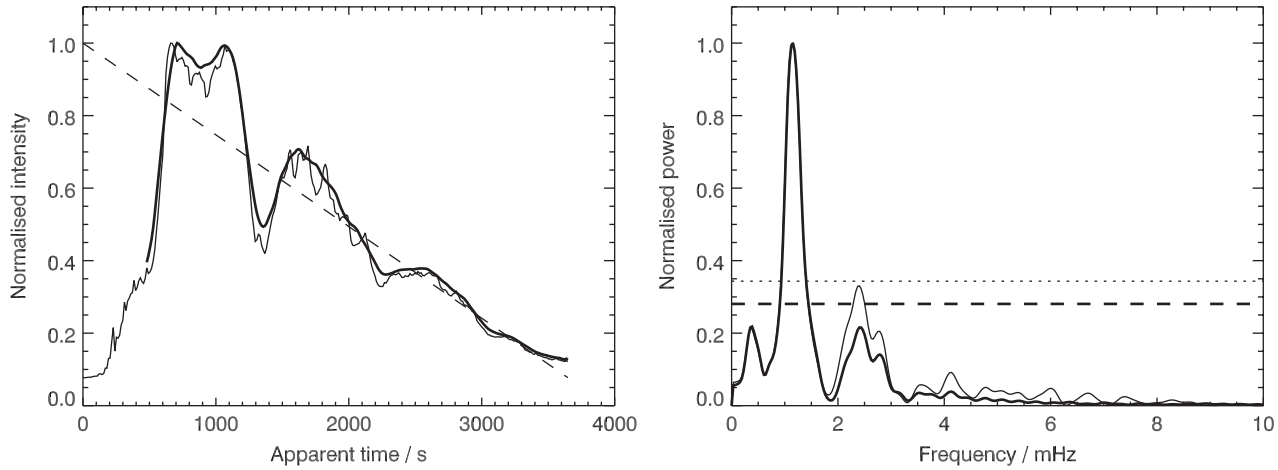


**Figure 3.** Left panel shows the time profile of maximum counts obtained in the AIA 335 Å channel in the flare loops (thin curve), and its box-car smoothing by 180 s (thick curve). The start time of the signal is 23:50:05 UT on 2010 November 4. The dashed line is the linear trend determined by the least-squares approximation. The right panel shows the power spectra of the detrended original signal (thin curve) and of the detrended smoothed signal (thick curve) obtained with a periodogram. The horizontal straight lines show the 99.99% confidence levels of the main spectral peaks for the detrended smoothed signal (thick dashed curve) and the detrended original signal (thin dotted curve). The confidence levels were calculated according to the recipe given in Horne & Baliunas (1986).

The path on the line of sight ($z$) is assumed to be half of the distance between footpoints of the flare loops seen in the contour in Figure 2(b) ($z = 25$ Mm). Substituting these observational results to Equation (2), we derived the EM and then estimated the number density of electrons at the top of the flare loops. The middle panel of Figure 4 shows the resulting electron density variation with time during the whole flare process. Since the peak emission of the flare is not caused by the thermal free–free but by the strong gyrosynchrotron emission, the density estimation related with the flare peak time cannot be analyzed as a physical parameter in our assumptions. Therefore we have examined the density estimated from 00:00 UT (the vertical dashed line in Figure 4) to 00:50 UT, from the time when the emission only comes from the free–free transition to just before the next flare start. From 00:00 UT, the density fluctuations come into sight and its amplitude gradually diminishes with time.

## 4. DECAYING OSCILLATIONS

The time dependence of the electron density derived by the radio emission (the middle panel of Figure 4), as well as the intensity in the EUV emission (Figure 3), shows a decaying long-period oscillatory pattern. Since the observational curve has a nonlinear trend, to emphasize the oscillatory pattern, we detrend the observational curve by subtracting its cubic parabolic trend. Best-fitting the detrended observational curve from 00:00 UT by a decaying harmonic function

$$s(t) = A \exp(-t/t_D) \sin(2\pi t/P + \phi_0), \quad (3)$$

where $A$, $t_D$, $P$, and $\phi_0$ are the amplitude, decay time, period, and initial phase, respectively, gives us the parameters of this oscillation: the period $P \approx 760$ s and the decay time $t_D \approx 900$ s. The amplitude of the oscillation is about 6% of the background in the beginning of the oscillations. The result

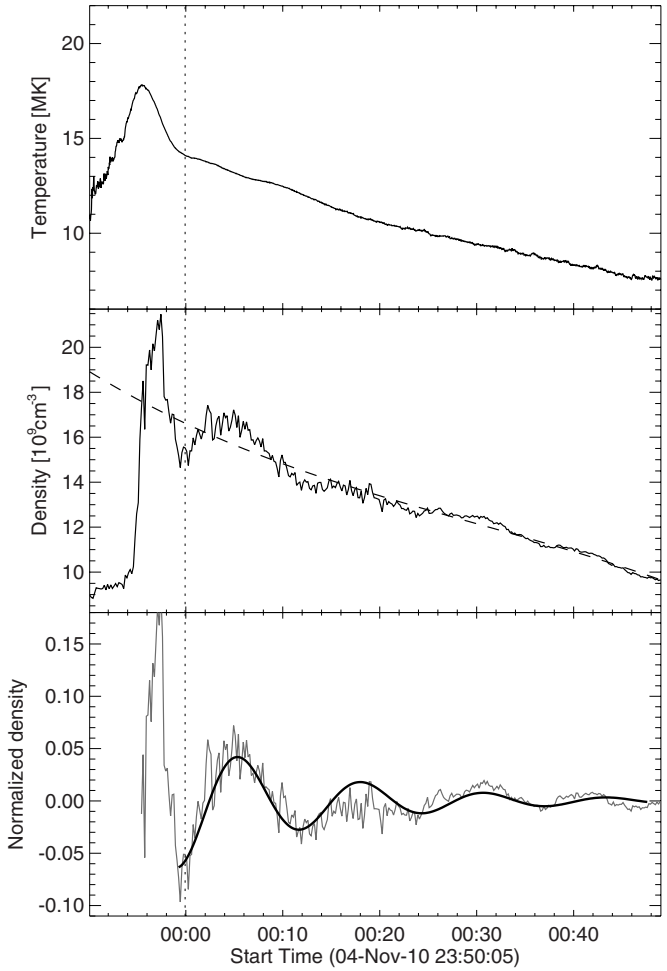


**Figure 4.** Top panel: time profile of temperature estimated by *GOES* two channels. Middle panel: electron number density derived by this temperature and $T_B$ at 17 GHz. Dashed line is the cubic parabolic trend. Bottom panel: the normalized electron number density (thin curve) and a best fit on it (thick curve). Free–free emission become more predominant than gyrosynchrotron emission from 00:00 UT on 2010 November 5 (vertical dotted line).

of this approximation, shown in the bottom panel of Figure 4, demonstrates a rather good agreement between the observational and the best-fitted curve. Also, we see that the amplitude of short-period fluctuations from this decaying harmonic curve decreases with time. We would like to stress that the detection of the oscillation is not sensitive to the specific choice of the time scale in the boxcar detrending, as the oscillatory pattern is clearly visible in the original signal.

## 5. DISCUSSION

We have demonstrated that there is an electron density QPP oscillation with a 12.6 minute period and 15 minute decay time, and the amplitude of several percent of the background in the flare loops. This electron density has been deduced by radio emission observed by the 17 GHz Nobeyama Radioheliograph and it is the first evidence of radio observation for the long-period oscillation of the thermal emission produced by a flare. The QPP is also well pronounced in the EUV 335 Å signal obtained with *SDO*/AIA, while the period is a bit longer, 13.8 minutes. The observed parameters of the oscillation, the period, and decay time, as well as its compressive nature, are similar to the compressive oscillations of coronal loops, known as SUMER oscillations.

Following the interpretation of SUMER oscillations as a standing slow magnetoacoustic wave (Ofman & Wang 2002) we estimate parameters of the observed oscillation. Consider two lowest spatial harmonics. Numerical simulations (e.g., Mendoza-Briceño et al. 2004; Tsiklauri et al. 2004) show that either of them is excited most effectively depending upon the initial driver. In the slow wave the density is perturbed because of the spatial redistribution of the matter mainly along the magnetic field. In a loop it corresponds to the field-aligned movement of the plasma from one footpoint to the other (in the fundamental mode) or from both the footpoint to the apex (in the second standing harmonics). Taking the loop height of about 50″ and assuming that the loop is of semi-circular shape, we get its length of about 115 Mm. The fundamental mode has the wavelengths of $\lambda_1 \approx 2 \times 115$ Mm. The wavelength of the second spatial harmonics is $\lambda_2 \approx 115$ Mm. Estimating the phase speeds as the ratio of the wavelengths to the value of the period, 760 s, we obtain about 300 km s$^{-1}$ for the fundamental mode and 150 km s$^{-1}$ for the second spatial harmonics. The plasma temperature associated with the 335 Å channel is about 2.5 MK, which gives us the sound speed of about $C_s \approx 240$ km s$^{-1}$. This value is consistent with the phase speed required for the interpretation of the oscillations in terms of the fundamental acoustic mode (see, e.g., Wang et al. 2007).

On the other hand, temperature diagnostics performed with the use of *GOES* data shows that the plasma has higher temperature, about 7 MK (see Section 3). For this temperature, the sound speed $C_s$ is greater than 380 km s$^{-1}$. In this case, the decrease in the phase speed can be attributed to the relatively low value of the Alfvén speed, $C_A$, and of the value of the sound speed. This reduces the phase speed of the longitudinal waves $C_T$ to the required value if $C_A \approx C_s$. This result is consistent with the estimations of the plasma beta (Shibasaki 2001, 2008), which show that in flaring loops this parameter could reach or even exceed unity, giving us the tube speed of the required value. The fact that the oscillations are clearly seen in the 335 Å channel can be attributed to the effect of the crosstalk from the 131 Å channel (Boerner et al. 2012). The oscillation is not seen in hotter channels of AIA because of the saturation.

Also, if the oscillation of the emission detected in the 335 Å channel is produced by the cooler plasma, this oscillation can be induced by the slow magnetoacoustic oscillations in the hotter loops. One possible scenario is based upon the possibility that hot and cool loops form loop bundles, with the steep temperature gradient in the transverse direction (e.g., King et al. 2003). Slow magnetoacoustic oscillations cause not only longitudinal, but also transverse motions of the plasma (Gruszecki & Nakariakov 2011). These transverse motions grow with the increase in beta, and are significant when beta is about unity. Hence, standing slow magnetoacoustic oscillations channeled by hotter loops would naturally affect the cooler plasma in the cooler loops situated nearby, and hence may be visible in the cooler temperature emission. The possible transfer of wave energy from mainly longitudinal modes to mainly transverse modes is an important issue for coronal energetics and magnetic connectivity. However, the observational evidence of this effect is scarce (e.g., McAteer et al. 2003; Srivastava & Dwivedi 2010, and references therein), and the present study does not provide us with a solid evidence of this effect either.

Thus, we conclude that our results give the first direct observational evidence of slow magnetoacoustic waves in the solar corona in the thermal radio emission, similar to the phenomenon known as SUMER oscillations. The slight difference in the

periods of the oscillations determined with NoRH and AIA, of about 17%, can be attributed to the different temperatures of the oscillating plasmas (and hence the sound and tube speeds), which is also consistent with the interpretation in terms of slow magnetoacoustic waves. The observed strong decay of the slow magnetoacoustic oscillations was shown to be caused by field-aligned thermal conduction (e.g., Ofman & Wang 2002). The second harmonics of the main period of the detected oscillation, 2.4 mHz, can be associated with the second harmonics of the main oscillation.

The observed gradual decrease in the electron density fluctuations from the decaying harmonic pattern can be attributed to the decay of the compressible turbulence in the flaring site, excited by the flare, and should be subject to further investigation.

V.M.N. was supported by the JSPS Invitation Fellowship S-11026 and the Royal Society International Project grant. Nobeyama radioheligraph and polarimeters are operated by the National Astronomical Observatory of Japan (NAOJ)/ Nobeyama Solar Radio Observatory (NSRO). The *GOES* satellite is operated by the National Oceanographic & Atmospheric Administration (NOAA). *SDO* is the first mission to be launched for NASA's Living With a Star (LWS) Program. The authors are grateful to the anonymous referee for valuable comments.

## REFERENCES

Boerner, P., Edwards, C., Lemen, J., et al. 2012, Sol. Phys., 275, 41
Chen, P. F., & Priest, E. R. 2006, Sol. Phys., 238, 313
Dere, K. P., Landi, E., Mason, H. E., Monsignori Fossi, B. C., & Young, P. R. 1997, A&AS, 125, 149
Dere, K. P., Landi, E., Young, P. R., et al. 2009, A&A, 498, 915
Dulk, G. A. 1985, ARA&A, 23, 169
Gruszecki, M., & Nakariakov, V. M. 2011, A&A, 536, A68
Horne, J. H., & Baliunas, S. L. 1986, ApJ, 302, 757
King, D. B., Nakariakov, V. M., Deluca, E. E., Golub, L., & McClements, K. G. 2003, A&A, 404, L1
Lemen, J. R., Title, A. M., Akin, D. J., et al. 2012, Sol. Phys., 275, 17
Mariska, J. T. 2005, ApJ, 620, L67
Mariska, J. T. 2006, ApJ, 639, 484
Mariska, J. T., Warren, H. P., Williams, D. R., & Watanabe, T. 2008, ApJ, 681, L41
Mathioudakis, M., Seiradakis, J. H., Williams, D. R., et al. 2003, A&A, 403, 1101
McAteer, R. T. J., Gallagher, P. T., Williams, D. R., et al. 2003, ApJ, 587, 806
Mendoza-Briceño, C. A., Erdélyi, R., & Sigalotti, L. D. G. 2004, ApJ, 605, 493
Mitra-Kraev, U., Harra, L. K., Williams, D. R., & Kraev, E. 2005, A&A, 436, 1041
Nakajima, H., Nishio, M., Enome, S., et al. 1994, Proc. IEEE, 82, 705
Nakajima, H., Sekiguchi, H., Sawa, M., Kai, K., & Kawashima, S. 1985, PASJ, 37, 163
Nakariakov, V. M., & Melnikov, V. F. 2006, A&A, 446, 1151
Nakariakov, V. M., & Melnikov, V. F. 2009, Space Sci. Rev., 149, 119
Nakariakov, V. M., Tsiklauri, D., Kelly, A., Arber, T. D., & Aschwanden, M. J. 2004, A&A, 414, L25
Ofman, L., & Wang, T. 2002, ApJ, 580, L85
Ogrodowczyk, R., & Murawski, K. 2007, A&A, 467, 311
Pandey, J. C., & Srivastava, A. K. 2009, ApJ, 697, L153
Roberts, B. 2006, Phil. Trans. R. Soc. A, 364, 447
Scargle, J. D. 1982, ApJ, 263, 835
Selwa, M., Murawski, K., & Solanki, S. K. 2005, A&A, 436, 701
Selwa, M., Ofman, L., & Murawski, K. 2007, ApJ, 668, L83
Shibasaki, K. 2001, ApJ, 557, 326
Shibasaki, K. 2008, Plasma Fusion Res., 2, 1012
Srivastava, A. K., & Dwivedi, D. N. 2010, New Astron., 15, 8
Stepanov, A. V., Kliem, B., Zaitsev, V. V., et al. 2001, A&A, 374, 1072
Takano, T., Nakajima, H., Enome, S., et al. 1997, in Proc. CESRA Workshop, Coronal Physics from Radio and Space Observations, ed. G. Trottet (Berlin: Springer), 185
Taroyan, Y., Erdélyi, R., Doyle, J. G., & Bradshaw, S. J. 2005, A&A, 438, 713
Tsiklauri, D., Nakariakov, V. M., Arber, T. D., & Aschwanden, M. J. 2004, A&A, 422, 351
Wang, T. 2011, Space Sci. Rev., 158, 397
Wang, T., Innes, D. E., & Qiu, J. 2007, ApJ, 656, 598
Wang, T. J., Solanki, S. K., Curdt, W., et al. 2003a, A&A, 406, 1105
Wang, T. J., Solanki, S. K., Innes, D. E., Curdt, W., & Marsch, E. 2003b, A&A, 402, L17
White, S. M., Thomas, R. J., & Schwartz, R. A. 2005, Sol. Phys., 227, 231